Check for updates

ADVANCED MATERIALS TECHNOLOGIES
www.advmattechnol.de

Pneumatic Enabled Vertical Interconnect Access of Liquid Alloy Circuits toward Highly Integrated Stretchable Electronics

*Qin Jiang, Shuo Zhang, Jiajun Jiang, Wenjie Fei, and Zhigang Wu**

Multilayer circuits, particularly in stretchable electronics, are always considered as an effective way to integrate diverse components and modules for advanced/powerful functions required in the potential applications or complex scenarios. As a desirable soft conductor, liquid alloy circuits exhibit super compliance and stretchability. However, the lacking of reliable ways to fabricate multilayer circuits like other stretchable electronics, the advantage of liquid alloy stretchable electronics is far away well exploited, especially from the perspectives of application developments. Here, based on the unique features of rapid oxidation and fluidity from liquid alloy, a facile method is presented to achieve multilayer circuits connection with vertical interconnect accesses enabled by pneumatic blowing and surface topography tuning. This approach provides a new way to achieve high integration of liquid alloy based stretchable electronics, for example, a double-layer soft LED array, a conformal six-layer wireless charging, and a wireless communicated wearable device for temperature and humidity real-time monitoring. Furthermore, compatible with conventional industry process, it may open a new window for making advanced or powerful liquid alloy stretchable electronics for various applications in complex scenarios.

1. Introduction

Stretchable electronics have been developed tremendously over the past decades due to the compliant mechanical deformability and electrical reliability. It can be employed in a wide range of dynamic and complex conditions that requiring multifunction as well as good conformability, such as human-machine interfaces,[1] soft robotics,[2–4] epidermal[5–7] and wearable electronics[8,9] for health monitoring.[10,11] To adapt to increasingly complex scenarios, plenty of functional components are integrated and encapsulated into stretchable/soft electronics for monitoring and acquiring signals. As the complexity of circuit design increases, using single-layer circuit layouts is not suitable for modular integration and miniaturization, which impedes the development of stretchable electronics. One of the most effective ways to improve the integration thus multifunction, is laminating multilayer circuits connected by vertical interconnect accesses (VIAs). Many approaches have been proposed to achieve VIAs, including filling solder paste[12] or electroplating copper.[13,14] However, these methods involve complicated processing steps, many chemicals, and turn the VIA into a rigid state, therefore decreases the device's compliance significantly.

Owing to its low viscosity, high conductivity, and high fluidity,[15,16] liquid metal (e.g., Gallium-based alloy) is widely utilized in stretchable electronics as an ultra-flexible/stretchable interconnector. Meanwhile, the oxide layer of the liquid alloy (LA) helps decrease its surface tension and makes it possible to fabricate various LA patterns with several approaches, for example, masked printing,[17,18] inkjet printing,[19] direct 3D printing,[20,21] micro-contact printing,[22] roller pen printing,[23,24] laser patterning,[25,26] hydro-printing,[27–29] selective wetting,[30,31] screen printing,[32,33] spray deposition,[34,35] and injection into microfluidic channels.[36,37] However, the LA-based circuits mostly remain limited to single layers and hence a simple function. Lacking reliable and efficient methods for massive integration and hence the support from many available powerful functional components/modules, the single layer formed circuit seriously limits the development of LA stretchable electronics from many aspects. Although there are a few approaches, for example, via a freestanding LA trace alignment[38–40] or reconfiguration[41] and a soft insulating layer,[2,42] were employed to fabricate cross and multilayer LA circuits, and they are not easy to control and incompatible to current industrial manufacturing. Recently, LA VIAs can also be achieved by combining with CO_2 laser ablation and LA spray deposition.[43] However, this work needs stencil masks, which require accurate alignment and the cone-shaped VIAs ablated by CO_2 laser are not desirable in electrical performance, especially in the high-frequency circuit.[44] Thus, efficient and industry-compatible processing of traces and VIAs are very important to achieve a stretchable multilayer LA device targeting more powerful performances and advanced functions in complex scenarios.

Recently, our team reported a flexography printing method for transfer printing LA circuits with high-fidelity and efficiency

Q. Jiang, S. Zhang, J. Jiang, W. Fei, Prof. Z. G. Wu
State Key Laboratory of Digital Manufacturing Equipment and Technology
School of Mechanical Science and Engineering
Huazhong University of Science and Technology
Wuhan 430074, China
E-mail: zgwu@hust.edu.cn

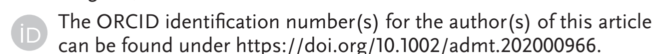
The ORCID identification number(s) for the author(s) of this article can be found under https://doi.org/10.1002/admt.202000966.

DOI: 10.1002/admt.202000966

 © 2021 Wiley-VCH GmbH

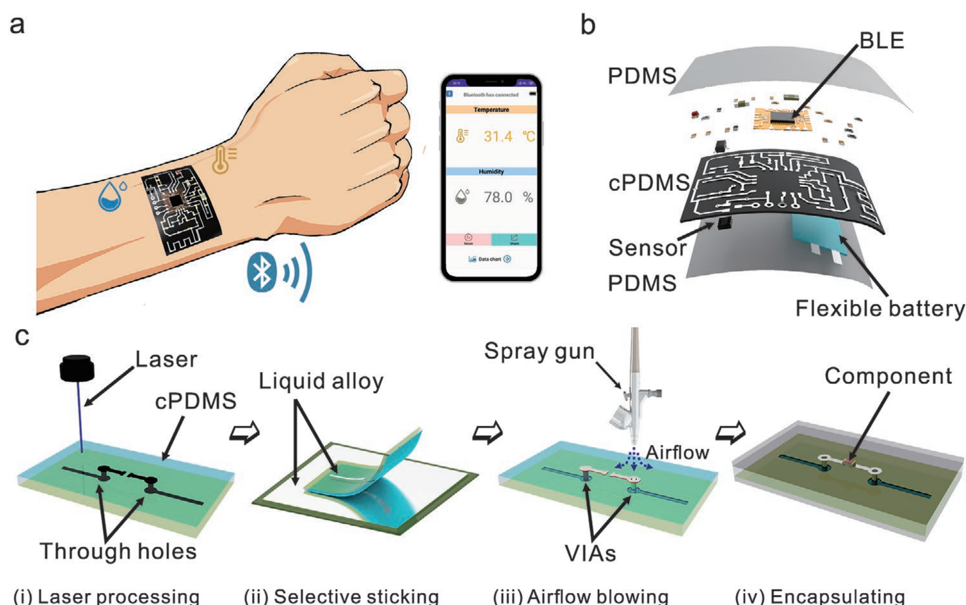

Figure 1. Design and fabrication process of the multilayer LA circuit. a) Schematic of a stretchable wearable health monitoring device. b) Exploded schematics of the wearable device. BLE, Bluetooth low energy; c) Brief illustration of the whole process: i) UV laser processing of the double-layer cPDMS surface to form patterns and through holes. ii) Selective sticking LA trace. iii) Electrical connection of the VIAs under airflow blowing. iv) Elastomeric encapsulation using PDMS.

via a selectively surface topography tuning.[45] However, it still focused on single-layer circuits without complex routing of LA trace, which severely limits the functionality of the made device.

Here, by pneumatic blowing thin layers of LA membranes between through holes on tuned surface topography, we report an efficient approach for fabricating multilayer stretchable electronics connected with interlayer VIAs. It leads to a higher integration density of components and more functional stretchable devices than using the single-layer approaches. Using such an approach, we demonstrated an all integrated conformal epidermis device for monitoring various psychological signals, for example, temperature and humidity, and communicating wirelessly with a mobile phone (**Figure 1**a). The device integrated Bluetooth low energy (BLE) SoC, sensor, surface mount devices (SMDs), and ultra-thin stretchable battery on the double-side of a carbon black-doped silicone substrate (Figure 1b).

2. Results and Discussion

2.1. Fabrication Process

A brief illustration of our implementation is shown in Figure 1c. The fabrication consists of three main steps. First, both surfaces of the soft substrate were selectively patterned by laser-scanning, and the through-holes were achieved by laser-ablating. After selectively pinning, the LA membranes were generated on both sides of holes due to the existence of oxide layer. Then, an airflow was employed to rupture the LA membranes (see the details in Video S1, Supporting Information). Owing to the adhesion and solidity of the oxide layer, the sputtered LA traces were re-connected to form VIAs. Finally, the circuit was encapsulated using soft elastomer.

2.2. Investigation on Fabrication and Mechanism of VIA

As shown in **Figure 2**a, we employ a UV laser to ablate the joint between circuits on both surfaces (here carbon doped Polydimethylsiloxane, cPDMS, for better light absorption in UV spectrum), forming a through-hole with a laser-ablated rough cross profile. The substrate matrix was ablated and cut, generating a vertical profile with micro/nanostructures[46] (Figure S1, Supporting Information). However, the micro/nanostructures can attract air effectively in the gaps, decreasing the effective contact area between the LA and the ablated surface. To learn more details on how the UV laser ablation can impact the surface morphology of the hole profile and wettability of LA on its surface, we conducted a series of experiments. As shown in Figure 2b, the surface roughness of the hole profile increased with increasing the laser scanning speed. The reason is that the laser spot overlap decreases with higher scanning speed, resulting in the continuity of the laser beam and laser energy density reducing (Figure S2, Supporting Information). Also, the weaker energy density was accompanied by a shallower ablation depth of the substrate. In such a case, it requires more repetitive scans to create a through-hole (at the scanning speed over 80 mm s^{-1}), which leads to a larger heat-affected zone. According to the previous studies,[29,46] the static contact angle of LA on the substrate relates to the surface roughness. The static contact angle of LA droplet on the UV-ablated hole section (≈160°) is larger than the scalpel cut cPDMS section (≈137°), indicating that the wettability of LA on the UV-ablated area was tuned from wetted to super-phobic (Figure S3, Supporting Information). We conducted a stick test, and the results showed that the UV-ablated section was more challenging to stick LA than the section cut by a scalpel (Figure S4, Supporting Information). Due to the low wettability of the LA on the hole

 © 2021 Wiley-VCH GmbH

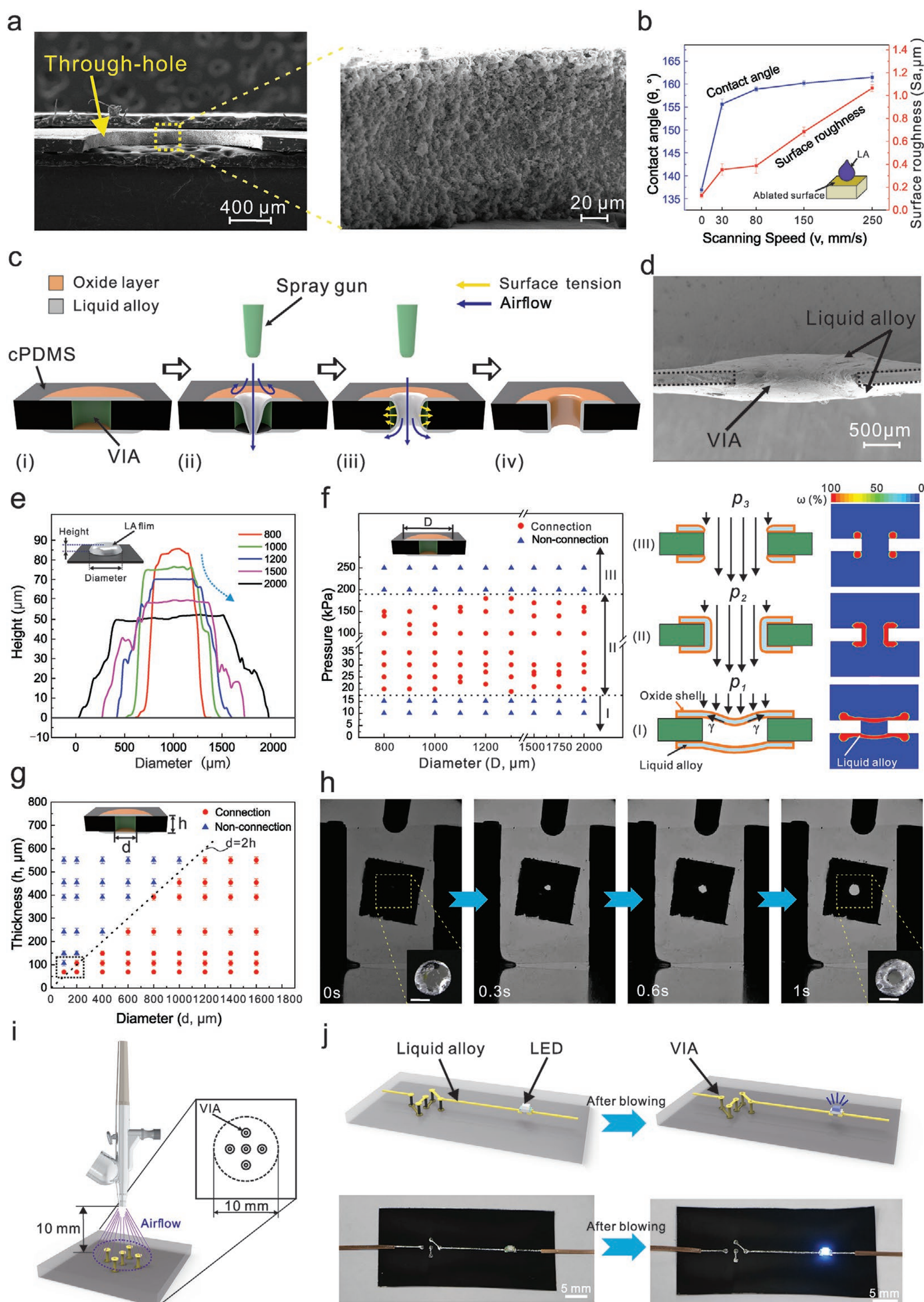

Figure 2. Fabrication and electrical connection of the VIAs. a) SEM images of UV laser-ablated through-hole surface morphology with a zoom-in view. b) Surfaces roughness of ablated surfaces and static contact angle of LA droplet on the surfaces with different laser scanning speeds (v). The laser scanning speed of 0 mm s^{-1} means that the surface is cut by a scalpel. c) Schematic process of LA connection formation in the VIA. d) SEM image of the LA connection in the VIA after airflow blowing. e) Height change of the LA membrane with different widths. f) VIAs connection states at different airflow pressure and membrane diameter (D), where p_1, p_2, p_3, the airflow force of acting on the LA membrane; γ, the surface tension of the LA membrane. The finite element analysis (FEA) showing the LA volumetric fraction (ω) distribution in three results under the airflow pressure: 15, 25, 200 kPa, respectively. g) The VIA connection states at different substrate thickness (h, μm) and diameter (d, μm) under 25 kPa air pressure blowing. h) images of a high-speed camera taking the VIA connection process. Scale bars = 2 mm. i) Schematic of pneumatic blowing for multiple VIAs simultaneously. j) Schematics (upper) and images (lower) of the circuit with five VIAs. After pneumatic blowing once, all the VIAs are formed, and the LED is lit on.

 © 2021 Wiley-VCH GmbH

section, it cannot remain stable, which indicates a LA interconnection cannot be pinned on the cross profile with its adhesive oxide layer.

To solve the above issue and achieve interconnection, we proposed a dynamic airflow blowing approach to form LA interconnection. As shown in Figure 2c(i), the through-hole was ablated and surrounded with an untreated pristine ring-like surface, where stick LA to generate two parallel membranes on both sides of the through-hole after selectively pinning LA. Subsequently, the oxide layer was instantly generated, resulting in the LA membrane maintaining its shape against surface tension and gravity. Then, on the condition of employing an airflow with a pressure larger than the LA's surface tension, the top LA membrane was partially destroyed and ruptured. Meanwhile, the rigid oxide skin broke during the blowing, which allows LA to regain its significant fluidity[47,48] and sputters along with the direction of airflow. Consequently, the sputtered LA membranes were contacted and connected with the bottom LA membrane due to the adhesion of the solid oxide layer (Figure 2c(ii)). With continuous pneumatic flowing, the re-connected LA contracted toward the profile under its surface tension (Figure 2c(iii)). Finally, a VIA was obtained under the presence of the airflow (Figure 2c(iv)). In addition, from the scanning electron microscope (SEM) view in Figure 2d and elemental mapping in Figure S5, Supporting Information, a universal and compliant LA membrane was observed to cover the profile surface of VIA, indicating an effective interconnection.

As shown in Figure 2e, the height of the LA membrane was related to the diameter of the untreated ring, and it slightly decreased from ≈85 to ≈50 µm as the diameter increase. To learn the height and employed air pressure on the connectivity of VIAs, we tested different air pressure as well as the diameter of the untreated ring (Figure 2f). From the results, it is found that there are three thresholds for pressure, corresponding to three different cases: I) The air pressure is too weak to overcome the surface tension and rupture the membrane ($p_1 < \gamma$); II) The suitable airflow pressure range (20–180 kPa) for a stable interconnection in the VIA; III) The air pressure is too strong that the interconnection is blown away. However, the diameter of the untreated ring (thickness of the LA membrane) did not influence the connectivity too much. What's more, we found that the airflow pressure we used does not show any observable influence on the nearby circuit due to the existence of the solid skin layer on the LA lines. Under 180 kPa of airflow pressure (the maximum pressure rank for VIA), the nearby circuit remained connected and kept intact (refer to the details in Video S2, Supporting Information). We also developed a finite element analysis for the membrane rupture under the airflow pressure (see the numerical analysis details in Note 1 and Figure S6, Supporting Information). Unlike other metals, conversion from rigid to fluid in the absence of oxide skin is LA's unique property.[49–51] Thus, the LA rheological behavior plays an important role in achieving VIA connection, affected by the oxide skin.

According to the previous study, the rupture location of the liquid membrane under vertical airflow blowing was near the membrane center.[52] Therefore, we investigated the relationship between the geometry of the hole and the connectivity. As shown in Figure 2g, when the diameter (d) is as twice as the thickness (h), the LA membrane was able to connect the through-hole. However, when the thickness was as thin as 69 ± 7 µm and 107 ± 12 µm, the hole was deformed under airflow, resulting in interconnectivity. Therefore, in the actual design, it is necessary to match the equation $d > 2h$, which is conducive to use the airflow blowing method to achieve VIA connection. We also captured the entire process of blowing by using the high-speed camera (Figure 2h).

Furthermore, this technology is scalable. By one operation, multiple VIAs can be achieved simultaneously, Figure 2i,j, within a small area (diameter < 10 mm) at the 10-mm distance from the blowing nozzle. With only one blowing, five VIAs were realized to connect the circuit and make it work, Figure 2j (the details in Video S3, Supporting Information). The results indicate that with a large area of laminar airflow, our approach can be adapted for massive VIAs in a short time for large-scale manufacture of stretchable circuits.

2.3. Electrical Characterization

To characterize the electrical property of the multilayer LA circuit fabricated by this approach, we conducted a series of experiments. We measured the variable resistance of LA circuits based on one single layer (I), double layers connected by one VIA (II), double layers connected by two VIAs and a 0 Ω resistor (III) (schematic illustration shown in **Figure 3**a–c, respectively). The LA trace was set with length of 30 mm and width of 500 µm; the diameter of the VIA was set as 300 µm. The footprints were connected externally by copper foils. After being encapsulated with PDMS, the specimens were cut into dumbbell shapes and mounted into a uniaxial tensile instrument for stretching test.

Figure 3d–f shows the relationship between strain and the resistance change rate for the above three cases. The average elongation at break for them was 96.7 ± 1.7%, 96.8 ± 1.6%, and 93.2 ± 3.7%, respectively. For sets II and III, the resistance change rates were lower than the theoretical relative change, which is based on the Resistance's Law (see the details in supporting Note 2, Supporting Information). We ignored the variation in the width of the LA traces and did not take into account the volume of LA contained inside the VIAs. The LA in the VIAs was squeezed out during the stretching and filled in the surface LA trace, which reduced the variation of the trace width and decreased the relative resistance change.

As shown in Figure 3g, a double-layer circuit connecting with an LED was stretched up to 50% strain and still functioned well. Also, we investigated the circuit performance during a cycling test. During the 1,500 cycles of stretching up to 50% strain, the resistance change remained stable (Figure 3h). Due to residual stresses in PDMS and cPDMS, the elastomer does not restore to its original length during the stretching and release process, which caused a small increase in resistance. The minimum and maximum resistance increased from 1.63 and 4.35 Ω to 1.85 and 4.65 Ω before and after the tensile test, respectively, with increments of 13.5% and 6.70%. During the process, the sample's resistance changed with a slight variation (0.2 Ω), which does not show any significant influence on the device's function. After the cycling test, the VIA's resistance

© 2021 Wiley-VCH GmbH

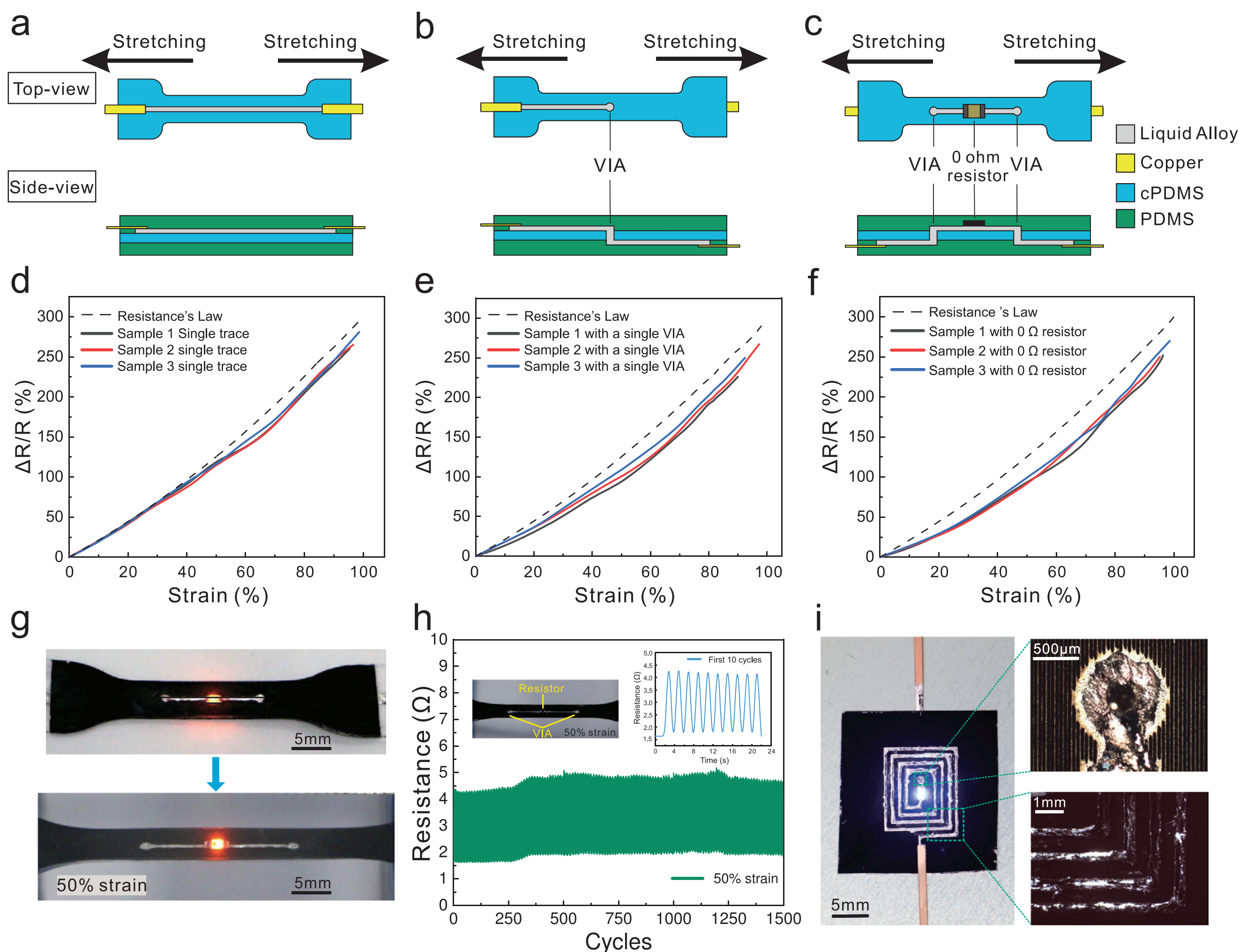

Figure 3. Electrical characterization of samples. Top-view and side-view schematic illustration of the specimens: a) Single LA trace on the top layer (set I). b) Single VIA connecting two LA traces (set II). c) SMD 0 Ω chip resistor integrating into the double-layer circuit (set III). Resistance change rate and strain curve: d) set I; e) set II; f) set III. g) Double-layer circuit integrated with LED from 0% strain to 50% strain. h) Measured resistance of set III specimens during the 1500 cycling test at 50% strain and 0.5 Hz. Inset: an image of the first ten times cycling test. i) Photographs of the rectangle coil circuit with zoomed-in views.

slightly increased from 0.1301 ± 0.0090 Ω to 0.1553 ± 0.0091 Ω, since LA within the VIA was partially squeezed out during the cycling. The tiny resistance change (≈0.025 Ω) has little influence on the entire circuit's resistance, indicating the VIA's good reliability under a dynamic stretch.

Although an interconnection VIA of 100 µm in diameter can be achieved by this method (Figure 2D), a thin cPDMS substrate (≈50 µm) is required. For ease handling of elastic substrate, we made a design parameter of 300 µm VIA diameter and ≈150 µm cPDMS substrate thickness. To test the circuit specification of this method, a rectangle coil circuit with a blue LED was made (Figure 3i). As shown in the zoom-in views, the diameter of VIA, width, and spacing of LA traces were ≈0.3, ≈0.3, and ≈0.4 mm, respectively. The result shows that the specification of our approach is compatible with those of conventional printed circuit board processes, which means that our method can meet the requirements of most circuit designs.

2.4. Demonstrations

Based on this approach, we fabricated a 25-LEDs array that could display different alphabets (**Figure** 4a). The LED components were placed on the top side and connected through 25 VIAs with the bottom side, suggesting good repeatability of the airflow blowing method. The array worked well under bending, twisting, and stretching, showing high flexibility and robustness (Video S2, Supporting Information). Further, a six-layer wireless charging device is demonstrated (Figure 4b). The device consists of three cPDMS substrates and six-layer circuits. In the middle, the cPDMS substrate was routed with the LA coil and generated the electric potential with the transmitter through electromagnetic induction. The VIAs were used for interlayer electrical connecting with the LEDs in the first and sixth layers. When the device approaches the transmitter coil, the LEDs can be illuminated (Video S3, Supporting Information). Also, we measured the power transfer efficiency of the

© 2021 Wiley-VCH GmbH

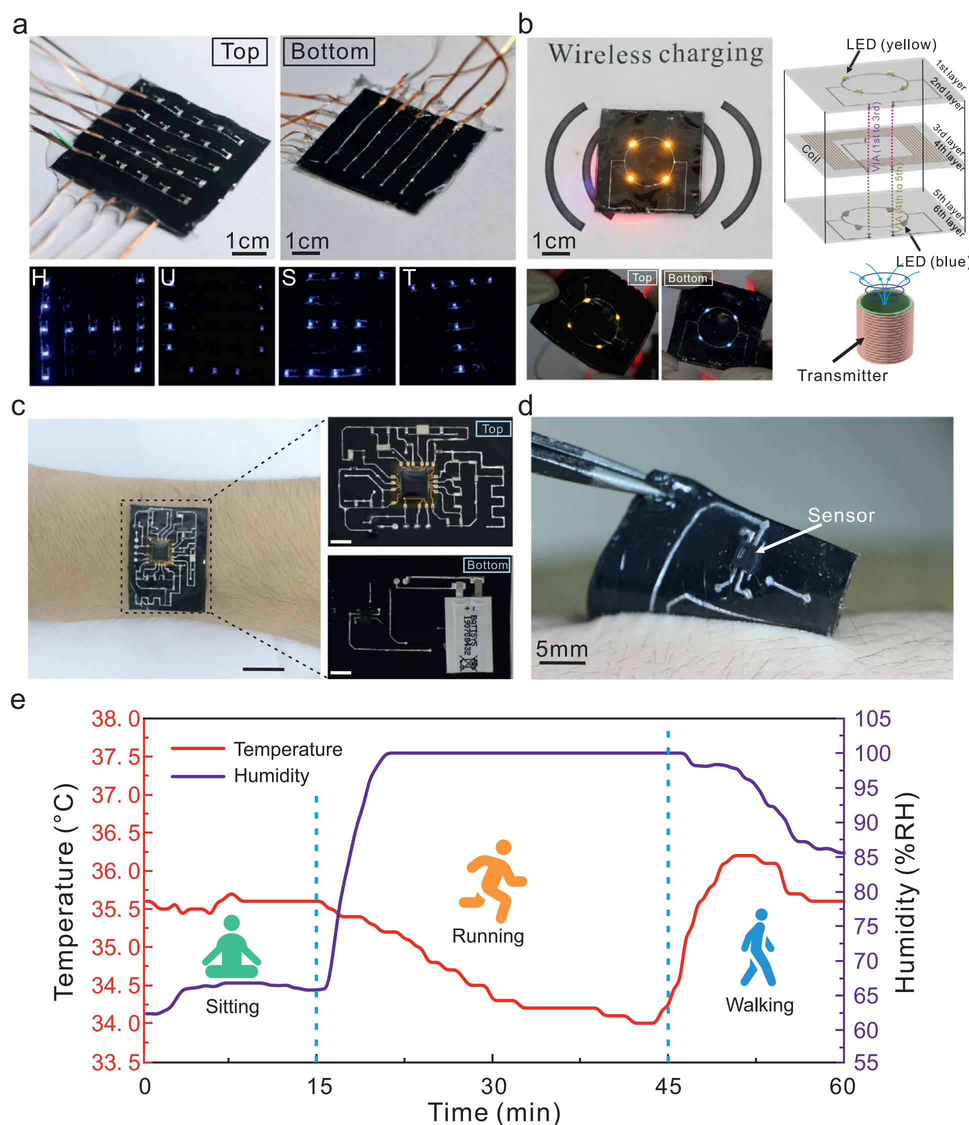

Figure 4. Demonstrations. a) Photographs of an LED array and display different alphabets during deformations. b) Explode schematics of the wireless charging device that is fabricated layer by layer. VIAs are used for interlayer electrical connection. The transmitter generates a high-frequency alternating magnetic field. c) Pictures showing the setup for temperature and humidity monitoring by placing the device on the forearm. The zoom-in views show the top and bottom sides of the device. Scale bars = 5 mm. d) Picture showing the device peeled off the skin. e) Real-time skin temperature and humidity variation data over 60 min under three movement conditions: sitting, running (at an average speed of 8 km h^{-1}), and walking (at an average speed of 4.5 km h^{-1}). The data measured every 30 s.

wireless transmission system (see the details in Note 3 and Figure S9, Supporting Information). The maximum power transfer efficiency could achieve 72% at a transmission distance of 2 mm. At this time, the receiver coil's equivalent voltage and power were up to 3.2 V and 0.8 W, respectively. Without any circuit optimization, its power transfer efficiency is a bit lower than that of current commercial rigid wireless charging devices.[53,54] However, it does demonstrate the applicability of our technology for multilayer circuit fabrication.

We fabricated an epidermal device for real-time monitoring of the psychological signals of temperature and humidity (Figure 4c). Twenty-five components with 11 VIAs were integrated into this device. The overall dimensions are approximately ($L \times W \times T$) $40 \times 25 \times 2.5$ mm^3. The total power budget of the device is around 6.4 mW (Figure S9, Supporting Information). By utilizing the ultra-thin flexible Li-ion battery (3 mAh), the device can work for ≈30 h with acquiring data every 10 min. The temperature and humidity sensor was directly contacted with the skin for accurate measurement (Figure 4D). To be conformably attached on the skin during dynamic and even harsh conditions, we used a 50:1 PDMS to increase the adhesion between the device and the skin. For communicating with the user interface, a soft Bluetooth antenna made of LA was employed. To investigate the radio bond variation during the deformation, we measured the corresponding coefficient of the antenna under different levels of strain (Figure S10,

© 2021 Wiley-VCH GmbH

Supporting Information). The antenna still works within the BLE radio band and maintains the reflection coefficient of more than 90% under 30% strain, which accommodated a diverse of dynamic motions (bending, twisting, and stretching) of human skin. Using Bluetooth communication, we can observe the real-time data with the user interface on a mobile phone (Video S4, Supporting Information). As shown in Figure 4e, the device was attached to a volunteer's forearm for monitoring the temperature and humidity within 1 h (Figure 4E). When sitting, the temperature and humidity of the volunteer at the relaxed state were ≈35.5 °C and ≈34.5 %RH, respectively. When the volunteer started running, the humidity increased up to almost ≈100 %RH because of sweating, while the temperature kept decreasing because the evaporation of sweat dissipated the heat during running. After running, the humidity started falling to ≈85 %RH, and the temperature increased to the normal level of ≈35.5 °C. The results demonstrate accurate monitoring and good contact with human movements. Potentially, this device could be used in the future for infant care, patient monitoring, and COVID-19 prevention.

3. Conclusions

In summary, by proposing a new fabrication technique of LA VIA, we presented multilayer LA circuits that enable route complex circuits and integrate high density of diverse components. Employing UV laser processing, we can fabricate LA circuit patterns and VIAs on soft substrate rapidly and efficiently. Owing to the unique fluidity, high deformability, and rapid oxidation of LA, we can achieve the electrical connection in the VIA by airflow blowing. The VIA can reach a diameter up to ≈100 µm and maintain the electrical properties stable under the deformation. We show the multilayer stretchable circuit applications such as a double-layer LED array, a six-layer wireless charging device, and a wearable health monitoring device, which is hard to be achieved by using the single-layer circuit. Further efforts will focus on automated manufacturing and further enhancing stretchable devices function.

4. Experimental Section

Pneumatic Blowing: A spray gun (Infinity CRplus 0.4, Harder und Steenbeck, Norderstedt, Germany) was utilized to blow the through-holes for achieving interconnections. The air outlet was pointed at H = 10 mm above the air-liquid interface (Figure S5b, Supporting Information). Nitrogen (N_2, 99.9% purity) was supplied from a gas cylinder through a precision pressure regulator (ML-500XII, MUSASHI, Japan) to the spray gun, controlling the air pressure and shot time of 1 s.

Stretchable Substrate Preparation: The cPDMS was prepared by mixing PDMS (Sylgard 184, Dow Corning Corporation) and carbon black (XC72R, CABOT, Alibaba) of 10:1:0.2 (silicon base/curing agent/carbon black). First, the carbon black and silicon base were stirred manually using a glass rod for 3 min and then stirred by a digital stirring (RW 20, IKA, Germany) at ≈1500 rpm for 3 min. Second, the curing agent was added to the mixture and stirred for 3 min. After vacuumed for removing bubbles, the mixture was filmed on the aluminum plate using a thin film applicator and then cured at 90 °C for 45 min in an oven (UF 55 plus, Memmert, Germany).

Fabrication of the Stretchable Device: The fabrication can be summarized into three parts: 1) circuits patterning; 2) VIAs connecting; 3) stretchable elastomeric packaging (Figure S7, Supporting Information). A square cPDMS substrate was cut by a scalpel and placed on a PET film to hold its shape. After that, a UV laser marker system (HGL-LSU3/5EI, Huagong Laser, Wuhan, China, wavelength: 355 nm, pulse repetition frequency: 50 kHz) was utilized to create the circuit pattern on the cPDMS substrate, following the CAD design file. The laser with a scanning speed of 600 mm s^{-1}, adjacent distance of 0.02 mm, pulse width of 0.1 µs and beam power of 0.872 W for surface treatment, and 30 mm s^{-1} scanning speed, 0.2 µs pulse width, and 3.710 W beam power for VIA ablation. After the double-sided pattern processing and cleaning with isopropanol, the cPDMS substrate was placed on a LA (Galinstan, 68.5% Ga, 21.5% In, 10% Sn, Geratherm Medical AG, Geschwenda, Germany) reservoir to stick the LA circuit selectively. Subsequently, using the same pneumatic blowing approach to achieve the VIA connection. Finally, the components were placed on the cPDMS substrate and encapsulated with PDMS (Sylgard 184, 10:1). Each side was cured at 100 °C for 30 min by a heat gun (858D, Yihua, Guangzhou, China).

Strategies for Laser Alignment: Mechanical laser alignment matched the double-side circuit patterns without offset, especially the VIAs. The PET's location holes were used to locate cPDMS substrate on an *XY*–axis precision manually platform (ShunRong, Shenzhen, China). The substrate center was aligned with the laser working center by adjusting this platform.

VIA Interconnection State Experiments: In the experiments shown in Figure 2f,g, the interconnection state of the VIA was examined by a digital multimeter (34461A, Keysight Technologies, USA) to measure its resistance. The connected VIA resistance was ≈0.3 ohm, while the disconnected VIA resistance was overload. In Figure 2g, several cPDMS substrates were scraped by film applicators (thickness level: 100, 150, 200, 400, 500, and 750 µm). Due to the viscosity of cPDMS, the actual coating thickness (h) of the substrate was inferior to the theoretical value. The substrate thickness was measured by a micrometer (iGaging, Shenzhen, China).

Stretching and Electrical Test: The test specimens were subject to uniaxial tensile loading on a dynamic mechanical test system (E1000, Instron, Boston) at a rate of 0.5 mm s^{-1} up to the failure of the specimen (Figure 3d–f). The cyclic mechanical loading tests were conducted using the dynamic mechanical test system through a program at 0.5 Hz (Figure 3h). The resistance of the specimens was measured by a digital multimeter (34, 461A, KeySight Technologies, Santa Rosa, CA, USA) at 10 Hz measurement frequency. The relative resistance changes were calculated by a MATLAB program (version 2018a, MathWorks, Natick, MA).

Surface Characterization: The roughness of the ablated section surface (Figure 2B) was calculated by an ultra-depth 3D microscope (DSX 510, Olympus, Japan). The surface morphologies of the ablated section surface and the surface element analysis of the VIA was characterized by a SEM (FSEM, GeminiSEM300, Carl Zeiss, Germany). The static contact angle was measured by drop shape analysis equipment (DSA25, KRUSS, Germany) with the sessile drop method. The LA droplet (4 µL) was dropped on the ablated surface (≈4 mm width) via a syringe pump (PUMP 11 ELITE Nanomite, Harvard Apparatus, Holliston, MA) at room temperature.

Demonstrated Devices Characterization: Three stretchable devices were demonstrated to represent this fabrication technology. The details of the design information can be found in the Supporting Method, Supporting Information.

All experiments complied with guidelines by the Huazhong University of Science and Technology. All subjects were volunteers (co-authors of the work) and provided informed consent.

Supporting Information

Supporting Information is available from the Wiley Online Library or from the author.

© 2021 Wiley-VCH GmbH

Acknowledgements

The materials based on the work was partly financially supported by National Science Foundation of China (U1613204), the "Guangdong Innovative and Entrepreneurial Research Team Program" under contract no. 2016ZT06G587. The general characterization facilities were partly provided by the Flexible Electronics Manufacturing Laboratory in Comprehensive Experiment Center for Advanced Manufacturing Equipment and Technology at Huazhong University of Science and Technology.

Conflict of Interest

The authors declare no conflict of interest.

Keywords

multilayer liquid alloy circuits, pneumatic blowing, rheological behavior, stretchable electronics, vertical interconnect access

Received: September 27, 2020
Revised: December 3, 2020
Published online: February 10, 2021

[1] L. Xu, S. R. Gutbrod, A. P. Bonifas, Y. Su, M. S. Sulkin, N. Lu, H.-J. Chung, K.-I. Jang, Z. Liu, M. Ying, C. Lu, R. C. Webb, J.-S. Kim, J. I. Laughner, H. Cheng, Y. Liu, A. Ameen, J.-W. Jeong, G.-T. Kim, Y. Huang, I. R. Efimov, J. A. Rogers, *Nat. Commun.* **2014**, *5*, 3329.
[2] T. N. Do, H. Phan, T. Nguyen, Y. Visell, *Adv. Funct. Mater.* **2018**, *28*, 1800244.
[3] J. Byun, Y. Lee, J. Yoon, B. Lee, E. Oh, S. Chung, T. Lee, K. J. Cho, J. Kim, Y. Hong, *Sci. Rob.* **2018**, *3*, eaas9020.
[4] C. M. Boutry, M. Negre, M. Jorda, O. Vardoulis, A. Chortos, O. Khatib, Z. Bao, *Sci. Rob.* **2018**, *3*, eaau6914.
[5] D.-H. Kim, N. Lu, R. Ma, Y.-S. Kim, R.-H. Kim, S. Wang, J. Wu, S. M. Won, H. Tao, A. Islam, K. J. Yu, T. Kim, R. Chowdhury, M. Ying, L. Xu, M. Li, H.-J. Chung, H. Keum, M. McCormick, P. Liu, Y.-W. Zhang, F. G. Omenetto, Y. Huang, T. Coleman, J. A. Rogers, *Science* **2011**, *333*, 838.
[6] T. Ha, J. Tran, S. Liu, H. Jang, H. Jeong, R. Mitbander, H. Huh, Y. Qiu, J. Duong, R. L. Wang, P. Wang, A. Tandon, J. Sirohi, N. Lu, *Adv. Sci.* **2019**, *6*, 1900290.
[7] S. H. Jeong, S. Zhang, K. Hjort, J. Hilborn, Z. G. Wu, *Adv. Mater.* **2016**, *28*, 5830.
[8] S. Choi, H. Lee, R. Ghaffari, T. Hyeon, D. H. Kim, *Adv. Mater.* **2016**, *28*, 4203.
[9] M. Amjadi, K. U. Kyung, I. Park, M. Sitti, *Adv. Funct. Mater.* **2016**, *26*, 1678.
[10] H. U. Chung, B. H. Kim, J. Y. Lee, J. Lee, Z. Xie, E. M. Ibler, K. H. Lee, A. Banks, J. Y. Jeong, J. Kim, C. Ogle, D. Grande, Y. Yu, H. Jang, P. Assem, D. Ryu, J. W. Kwak, M. Namkoong, J. Bin Park, Y. Lee, D. H. Kim, A. Ryu, J. Jeong, K. You, B. Ji, Z. Liu, Q. Huo, X. Feng, Y. Deng, Y. Xu, et al, *Science* **2019**, *363*, eaau0780.
[11] C. Wang, X. Li, H. Hu, L. Zhang, Z. Huang, M. Lin, Z. Zhang, Z. Yin, B. Huang, H. Gong, S. Bhaskaran, Y. Gu, M. Makihata, Y. Guo, Y. Lei, Y. Chen, C. Wang, Y. Li, T. Zhang, Z. Chen, A. P. Pisano, L. Zhang, Q. Zhou, S. Xu, *Nat. Biomed. Eng.* **2018**, *2*, 687.
[12] Z. Huang, Y. Hao, Y. Li, H. Hu, C. Wang, A. Nomoto, T. Pan, Y. Gu, Y. Chen, T. Zhang, W. Li, Y. Lei, N. Kim, C. Wang, L. Zhang, J. W. Ward, A. Maralani, X. Li, M. F. Durstock, A. Pisano, Y. Lin, S. Xu, *Nat. Electron.* **2018**, *1*, 473.
[13] S. Biswas, A. Schoeberl, Y. Hao, J. Reiprich, T. Stauden, J. Pezoldt, H. O. Jacobs, *Nat. Commun.* **2019**, *10*, 1.
[14] T. Zhang, E. Asher, J. Yang, *Adv. Mater. Technol.* **2018**, *3*, 1700346.
[15] J. N. Koster, *Cryst. Res. Technol.* **1999**, *34*, 1129.
[16] M. D. Dickey, R. C. Chiechi, R. J. Larsen, E. A. Weiss, D. A. Weitz, G. M. Whitesides, *Adv. Funct. Mater.* **2008**, *18*, 1097.
[17] R. K. Kramer, C. Majidi, R. J. Wood, *Adv. Funct. Mater.* **2013**, *23*, 5292.
[18] S. H. Jeong, A. Hagman, K. Hjort, M. Jobs, J. Sundqvist, Z. Wu, *Lab Chip* **2012**, *12*, 4657.
[19] K. H. Choi, J. T. Yoo, C. K. Lee, S. Y. Lee, *Energy Environ. Sci.* **2016**, *9*, 2812.
[20] Y. Zheng, Z. Z. He, Y. Gao, J. Liu, *Sci. Rep.* **2013**, *3*, 1.
[21] J. W. Boley, E. L. White, G. T. C. Chiu, R. K. Kramer, *Adv. Funct. Mater.* **2014**, *24*, 3501.
[22] A. Tabatabai, A. Fassler, C. Usiak, C. Majidi, *Langmuir* **2013**, *29*, 6194.
[23] Y. Zheng, Z. Z. He, J. Yang, J. Liu, *Sci. Rep.* **2014**, *4*, 4588.
[24] Y. Zheng, Q. Zhang, J. Liu, *AIP Adv.* **2013**, *3*, 112117.
[25] T. Lu, L. Finkenauer, J. Wissman, C. Majidi, *Adv. Funct. Mater.* **2014**, *24*, 3351.
[26] T. Lu, E. J. Markvicka, Y. Jin, C. Majidi, *ACS Appl. Mater. Interfaces* **2017**, *9*, 22055.
[27] P. A. Lopes, H. Paisana, A. T. De Almeida, C. Majidi, M. Tavakoli, *ACS Appl. Mater. Interfaces* **2018**, *10*, 38760.
[28] G. Saada, M. Layani, A. Chernevousky, S. Magdassi, *Adv. Mater. Technol.* **2017**, *2*, 1600289.
[29] J. Jiang, S. Zhang, B. Wang, H. Ding, Z. Wu, *Small* **2020**, *16*, e2003833.
[30] G. Li, X. Wu, D. W. Lee, *Sens. Actuators, B* **2015**, *221*, 1114.
[31] Y. G. Moon, J. B. Koo, N. M. Park, J. Y. Oh, B. S. Na, S. S. Lee, S. D. Ahn, C. W. Park, *IEEE Trans. Electron Devices* **2017**, *64*, 5157.
[32] J. Tang, X. Zhao, J. Li, R. Guo, Y. Zhou, J. Liu, *ACS Appl. Mater. Interfaces* **2017**, *9*, 35977.
[33] Y. Li, S. Feng, S. Cao, J. Zhang, D. Kong, *ACS Appl. Mater. Interfaces* **2020**, *12*, 50852.
[34] Q. Zhang, Y. Gao, J. Liu, *Appl. Phys. A: Mater. Sci. Process.* **2014**, *116*, 1091.
[35] K. Zhang, S. Kong, Y. Li, M. Lu, D. Kong, *Lab Chip* **2019**, *19*, 2709.
[36] Y. L. Park, B. R. Chen, R. J. Wood, *IEEE Sens. J.* **2012**, *12*, 2711.
[37] Y. Gao, H. Ota, E. W. Schaler, K. Chen, A. Zhao, W. Gao, H. M. Fahad, Y. Leng, A. Zheng, F. Xiong, C. Zhang, L. C. Tai, P. Zhao, R. S. Fearing, A. Javey, *Adv. Mater.* **2017**, *29*, 1701985.
[38] S. Cheng, Z. Wu, *Lab Chip* **2010**, *10*, 3227.
[39] S. Cheng, Z. Wu, *Adv. Funct. Mater.* **2011**, *21*, 2282.
[40] S. H. Jeong, K. Hjort, Z. Wu, *Sci. Rep.* **2015**, *5*, 8419.
[41] Y. G. Park, H. S. An, J. Y. Kim, J. U. Park, *Sci. Adv.* **2019**, *5*, eaaw2844.
[42] J. Byun, B. Lee, E. Oh, H. Kim, S. Kim, S. Lee, Y. Hong, *Sci. Rep.* **2017**, *7*, 45328.
[43] D. Green Marques, P. Alhais Lopes, A. T. De Almeida, C. Majidi, M. Tavakoli, *Lab Chip* **2019**, *19*, 897.
[44] T. Kushta, K. Narita, T. Kaneko, T. Saeki, H. Tohya, *IEEE Microwave Wireless Compon. Lett.* **2003**, *13*, 169.
[45] S. Zhang, B. Wang, J. Jiang, K. Wu, C. F. Guo, Z. Wu, *ACS Appl. Mater. Interfaces* **2019**, *11*, 7148.
[46] S. Zhang, Q. Jiang, Y. Xu, C. F. Guo, Z. Wu, *Micromachines* **2020**, *11*, 682.
[47] R. K. Kramer, J. W. Boley, H. A. Stone, J. C. Weaver, R. J. Wood, *Langmuir* **2014**, *30*, 533.
[48] K. Doudrick, S. Liu, E. M. Mutunga, K. L. Klein, V. Damle, K. K. Varanasi, K. Rykaczewski, *Langmuir* **2014**, *30*, 6867.
[49] M. D. Dickey, *ACS Appl. Mater. Interfaces* **2014**, *6*, 18369.
[50] J. Wissman, M. D. Dickey, C. Majidi, *Adv. Sci.* **2017**, *4*, 1700169.
[51] K. B. Ozutemiz, J. Wissman, O. B. Ozdoganlar, C. Majidi, *Adv. Mater. Interfaces* **2018**, *5*, 1701596.
[52] C. W. J. Berendsen, J. C. H. Zeegers, G. C. F. L. Kruis, M. Riepen, A. A. Darhuber, *Langmuir* **2012**, *28*, 9977.
[53] J. Garnica, R. A. Chinga, J. Lin, *Proc. IEEE* **2013**, *101*, 1321.
[54] Z. Zhang, H. Pang, A. Georgiadis, C. Cecati, *IEEE Trans. Ind. Electron.* **2019**, *66*, 1044.

© 2021 Wiley-VCH GmbH